Applied Catalysis B: Environmental 91 (2009) 11–20

Contents lists available at ScienceDirect

Applied Catalysis B: Environmental

journal homepage: www.elsevier.com/locate/apcatb

Creation of three-dimensionally ordered macroporous Au/CeO_2 catalysts with controlled pore sizes and their enhanced catalytic performance for formaldehyde oxidation

Jun Zhang [a,*], Ying Jin [a], Changyan Li [a], Yuenian Shen [a], Li Han [b], Zhongxue Hu [a], Xiaowei Di [a], Zhiliang Liu [a]

[a] College of Chemistry and Chemical Engineering, Inner Mongolia University, Hohhot 010021, PR China
[b] Baotou Research Institute of Rare Earths, Baotou 014030, PR China

ARTICLE INFO

Article history:
Received 13 February 2009
Received in revised form 21 April 2009
Accepted 1 May 2009
Available online 9 May 2009

Keywords:
Three-dimensionally ordered macroporous Au/CeO_2 catalysts
Catalysis
Formaldehyde oxidation

ABSTRACT

Three-dimensionally ordered macroporous (3DOM) Au/CeO_2 catalysts with controlled pore sizes are successfully created via a colloidal crystal template method, and their enhanced catalytic performance for formaldehyde oxidation is systematically investigated for the first time in this paper. The resulting Au/CeO_2 catalysts possess well-defined 3DOM structures with adjustable pore sizes from 80 to 280 nm, having interconnected networks of spherical voids. Due to the uniform macroporous structures leading to good distribution of catalytic species of Au nanoparticles with less aggregation, the 3DOM Au/CeO_2 catalysts are expected to have enhanced capability for formaldehyde catalytic oxidation. The formaldehyde oxidation tests reveal that the 3DOM Au/CeO_2 catalysts exhibit superior catalytic activity with 100% formaldehyde conversion at ~75 °C, a much lower temperature than previously reported powder Au/CeO_2 catalysts. The superior performance of 3DOM Au/CeO_2 catalysts for formaldehyde oxidation makes them potentially applicable to in-door formaldehyde decontamination and industrial catalysis.

1. Introduction

It is well known that prolonged exposure to concentrations of formaldehyde that exceed safe limitations is greatly harmful to human health. According to the reports, serious health problems including burning sensations in the eyes and throat, nausea, difficulty in breathing, and even lethiferous diseases such as nasopharyngeal or nasal cancer can be caused if humans are exposed to an indoor environment polluted with elevated formaldehyde levels for an extended length of time [1–3]. House decorations made from materials with high formaldehyde content are a common source accounting for indoor air pollution [1]. Due to its health effects, formaldehyde pollution is currently of increasing concern.

Various methods have been developed to eliminate formaldehyde pollution. One effective method is the conversion of formaldehyde into carbon dioxide and water via formaldehyde catalytic oxidation. To realize this aim, efficient catalysts that can enhance formaldehyde oxidation at a moderate temperature are needed. So far, a variety of studies have been conducted seeking efficient catalysts with low cost and enhanced catalytic capability for formaldehyde oxidation. Several series of catalysts, such as noble metals (Pt, Pb, and Ru) [4,5], transition metal oxides (Fe_2O_3, MnO_2, NiO, and Co_3O_4) [6], rare earth or composite oxides (CeO_2, $LaMnO_3$, and $LaFeO_3$) [7,8], and oxide-supported noble metals (Ag/MnO_x-CeO_2, Pt/TiO_2, and Pt/MnO_2) [9–14], have been developed for formaldehyde catalytic oxidation. Noble metal catalysts usually show superior catalytic performance in relatively low temperatures, but they are quite expensive. Metal oxide catalysts have lower cost, but the temperature for catalytic conversion of formaldehyde is usually high at 200–300 °C, and their catalytic efficiency is inadequate. Oxide-supported noble metal catalysts are increasingly attractive because they show superior catalytic performance at moderate temperature and are relatively low cost [10,14]. For example, the Pd-MnO_x/Al_2O_3 catalyst has been recently reported by Álvarez-Galván et al. to show superior catalytic activity for complete formaldehyde oxidation at moderate temperatures around 80 °C [13–15], and Shen and co-workers has developed Ag/MnO_x-CeO_2 and Pt/MnO_x-CeO_2 catalysts, with which formaldehyde can be completely oxidized at 100 °C and ambient temperature, respectively [10,16].

Recently, remarkable research has been concentrated on studying the catalytic properties of ultrafine Au nanoparticles and oxide-supported Au catalysts, which are proven to exhibit extraordinarily high activity in many reactions including in formaldehyde catalytic oxidation at moderate temperatures

* Corresponding author. Tel.: +86 471 4993405; fax: +86 471 4993405.
E-mail address: cejzhang@imu.edu.cn (J. Zhang).

0926-3373/$ – see front matter © 2009 Elsevier B.V. All rights reserved.
doi:10.1016/j.apcatb.2009.05.001

[17–24]. Fe_2O_3- and CeO_2-supported Au catalysts have been recently found to show superior catalytic activity for formaldehyde oxidation [19,20]. The temperature required for 100% catalytic conversion of formaldehyde by these catalysts can be lowered to a moderate temperature of ~105 °C [20]. Oxide-supported Au catalysts, especially with CeO_2 supports, are therefore expected to be a valuable catalyst system for practical catalytic removal of formaldehyde. However, the temperature of formaldehyde oxidation with these catalysts needs to be further lowered.

It is commonly accepted that the aggregation of Au nanoparticles on powder catalyst supports during the preparation largely affect their catalytic activity, since the aggregation may lead to the formation of large particles and reduce the catalyst surface areas, eventually lowering their catalytic activity. Three-dimensional ordered macroporous (3DOM) materials show great merit for catalysis. They could be used as superior catalyst supports. As catalyst supports, 3DOM materials could afford unique porous geometry for key catalyst species loading. Less aggregation and good distribution of key catalyst species on 3DOM supports are desired, which would be beneficial for improving catalytic activity.

In this paper, novel 3DOM Au/CeO_2 catalysts were developed by in situ formation of Au nanoparticle catalysts onto 3DOM CeO_2 supports. The synthesis processes of polystyrene (PS) colloidal crystal assembly, 3DOM CeO_2 support formation, and 3DOM Au/CeO_2 catalyst fabrication were systematically studied, and the performance of 3DOM Au/CeO_2 catalysts with different pore sizes was tested for formaldehyde catalytic oxidation. It was found that 3DOM Au/CeO_2 catalysts showed enhanced catalytic activity for formaldehyde oxidation at moderate temperatures in comparison with previously reported Au/CeO_2 catalysts without porous structures. The enhanced activity of 3DOM catalysts may be attributed to the well-arranged 3DOM structures of Au/CeO_2 catalysts, which afford unique porous geometry for good distribution of small Au nanoparticles with less aggregation. The 3DOM catalysts have potential for a wide range of applications in indoor formaldehyde decontamination and industrial catalysis due to their enhanced catalytic property, low cost, and ability to be easily reused and recycled.

2. Experimentals and methods

2.1. Catalyst preparation

2.1.1. Synthesis of monodispersed PS colloidal spheres

The monodispersed PS colloidal spheres used as templates for the creation of 3DOM catalysts were synthesized by soap-free-emulsion polymerization or dispersion polymerization, depending on the sizes of PS colloidal spheres desired, according to literature methods with some modification. PS colloidal spheres with average diameters of 200, 400, and 600 nm were prepared via a soap-free-emulsion polymerization route [25–27]. The typical procedures for the preparation are as follows. Before preparation, styrene (St) monomer was washed with NaOH solution (0.1 M) and distilled water four times in a separatory funnel. Then, a certain amount of pre-treated St monomer and distilled water (see Table 1 for details) were added to a 250 mL three neck round-bottomed flask equipped with a condenser, a thermometer, and a pipe for nitrogen introduction. The mixture was magnetically stirred, and nitrogen was introduced to remove the air inside the flask and afford an inert reaction atmosphere. Next, following the addition of $K_2S_2O_8$ (KPS) solution (0.007 g/mL) to initiate polymerization, the temperature of the reaction system was raised to 70 °C. The polymerization reaction was conducted at 70 °C for 28 h. After the reaction was finished, the reaction system was naturally cooled to room temperature, and filtered to obtain the homogenous latex with nearly monodispersed PS particles. By varying the reaction conditions listed in Table 1, monodispersed PS colloidal spheres with average diameters around 200, 400, and 600 nm were achieved.

To obtain monodispersed PS colloid spheres with larger average diameters around 800 nm, the dispersion polymerization method was employed [28–31]. A typical sample was prepared as follows. To a 250 mL four neck round-bottomed flask equipped with an electric motor driving a glass stirring rod and Teflon wedge, a condenser, a thermometer, and a pipe for nitrogen introduction, a certain amount of polyvinylpyrrolidone (PVP), absolute ethanol and distilled water (see Table 1 for details) were added. The mixture was bubbled with nitrogen to remove the air inside the flask and afford an inert atmosphere. The reaction system was mechanically stirred at a rate of 120 rpm, heated to 70 °C with a water bath, and kept for further use. At the same time, a certain amount of St monomer and azobisisbutyronitrile (AIBN) were dissolved, and the solution was added to the four-neck flask under the same stirring and atmosphere conditions. After the system had been reacted for 12 h, the homogenous latex was obtained. The latex was centrifuged at a rate of 4000 rpm to collect the PS colloidal spheres by discarding the supernatant. The collected PS colloidal spheres were washed with absolute ethanol three times to completely remove the unreacted reactants and dispersion stabilizers. The final products of PS colloidal spheres were obtained by drying in a vacuum oven at 60 °C for 8 h.

2.1.2. Assembly of three-dimensionally ordered PS colloidal crystal templates

The three-dimensional ordered PS colloidal crystal templates were assembled via a centrifugation method [32]. A certain amount of PS latex consisting of monodispersed PS colloidal spheres was ultrasonicated to form a uniform emulsion and centrifuged at a rate of 1 krpm for 20 h. Depending on the sizes of the PS colloidal spheres, the centrifuging time could be slightly variable. After the PS colloidal spheres were fully precipitated, the supernatant was carefully removed using a dropper. The centrifuge

Table 1
Reaction conditions for synthesis of monodispersed PS colloidal spheres with different average diameters by soap-free-emulsion polymerization and dispersion polymerization methods.

Method	Soap-free-emulsion-polymerization					
St (mL)	$K_2S_2O_8$ (mL)	H_2O (mL)	Stirring speed (rpm)	Temperature (°C)	Time (h)	Average sphere diameter (nm)
6	10	170	120	70	28	200
10	10	170	120	70	28	400
20	10	170	120	70	28	600

Method	Disperse polymerization						
St (mL)	PVP (g)	AIBN (g)	EtOH/H_2O (mL)	Stirring speed (rpm)	Temperature (°C)	Time (h)	Average sphere diameter (μm)
6	1.0	0.1	95/10	120	70	12	0.8

tube containing the well-arranged PS colloidal spheres was then dried in an oven at 40 °C to obtain the final highly ordered three-dimensional PS colloidal crystal templates for use in synthesizing 3DOM CeO_2.

2.1.3. Synthesis of 3DOM CeO_2

The synthesis of 3DOM CeO_2 was carried out following a reported method with slight modification [33]. Equal molar citric acid (1.05 g) and $Ce(NO_3)_3{\cdot}6H_2O$ (2.17 g) were dissolved in ethanol (10 mL, 95%) to form a precursor solution. The citric acid was employed here to be a chelating ligand to form stable complex with rare earth ions, providing a higher melting point and a good compatibleness with PS template [34]. The three-dimensional ordered PS colloidal crystal templates were carefully placed into a Buchner funnel, to which a vacuum was applied. Then, the precursor solution was dropped into the funnel until the PS colloidal crystal templates were completely permeated. The PS colloidal crystal templates permeated with citric acid and $Ce(NO_3)_3$ precursor solution were then dried at 60 °C for 1.5 h. The above procedures were repeated four times to ensure the complete permeation of citric acid and $Ce(NO_3)_3$ precursor solution into the interstices of the PS colloidal crystal templates. The obtained PS colloidal crystal templates filled with citric acid and $Ce(NO_3)_3$ precursor solution were annealed at 500 °C at a heating rate of 3 °C/min for 5 h to remove the PS colloidal templates to form 3DOM CeO_2. Due to the shrinkage of the PS sphere templates during the calcination process, the pore sizes of the 3DOM CeO_2 supports prepared by using 200, 400, 600, and 800 nm PS spheres as templates were approximately 80, 130, 240, and 280 nm, respectively.

2.1.4. Synthesis of 3DOM Au/CeO_2 catalysts

The synthesis of 3DOM Au/CeO_2 catalysts was carried out via a gas bubbling-assisted deposition precipitation method developed in our lab. The typical preparative procedures were described as follows: 3DOM CeO_2 (0.2 g) supports with pore sizes of 80, 130, and 280 nm were introduced into $HAuCl_4$ solution. 4.2, 8.4, 12.6, and 16.8 mL $HAuCl_4$ solutions (1 g/L) diluted with 100 mL distilled water were used to prepare 3DOM Au/CeO_2 catalysts with theoretical Au content of 1, 2, 3, and 4 wt%, respectively. Since the normal magnetic stirring may destroy the 3DOM structures, the gas bubbling-assisted stirring operation with four output bubbling outlets in solution was developed to vigorously stir the solution to make the reaction homogenous and improve the uniform distribution of Au nanoparticles on the 3DOM CeO_2 supports. After bubbling the solution with air for 0.5 h, the pH was adjusted to 9 by adding Na_2CO_3 (0.2 mol/L) to precipitate the Au ions. The reaction system was further vigorously bubbled with air for 2 h, and let stand for 24 h. Then, the product was filtered and washed until the Cl^- was completely removed according to a test with $Ag(NO)_3$, and the final products were dried in an oven at 60 °C to obtain the desired 3DOM Au/CeO_2 catalysts with various pore sizes. To evaluate the effect of the annealing temperature on the catalytic performance for formaldehyde oxidation, as-dried 3DOM Au/CeO_2 samples were annealed at 200 and 400 °C.

2.2. Characterization

Powder X-ray diffraction (XRD) was used to characterize the phase structures of the catalysts. Measurements were performed using a Bruker AXS-D8 diffractometer (German) operated at 40 kV and 40 mA with a slit of 1/2 at a scanning rate of 3° min^{-1} in a scanning range of $2\theta = 20–80°$, using Cu Kα radiation ($\lambda = 0.15406$ nm). Samples for XRD were prepared by gently crushing the obtained products with a mortar and pestle and were placed in a quartz glass holder for characterization. Transmission electron microscopy (TEM) characterization was performed on a JEM-2010 system operated at an acceleration voltage of 120 kV to evaluate the structure, geometry, pore size, and Au distribution in the catalyst. Samples for TEM analysis were prepared by drying a drop of PS latex or catalyst dispersion on an amorphous carbon-coated copper grid for the observation. Scanning electron micrographs were recorded with a Hitachi S-3400N scanning electron microscope (SEM) to determine the PS sizes, colloidal crystal arrangement, and catalyst pore sizes. Samples for SEM measurements were deposited on silicon substrates and coated with a 5 nm Pt for characterization. Energy dispersive spectroscopy (EDS) was performed using an EDAX system attached to an SEM. Surface area measurements were performed on an ASAP 2010 Brunauer–Emmett–Teller (BET) analyzer. X-ray photoelectron spectroscopy (XPS) measurements were carried out on a XSAM800 X-ray photoelectron spectrometer with an Al Kα (1486.67 eV) excitation source to determine the existence and valence states of Au nanoparticles in the catalysts. Samples annealed at different temperatures were used for characterization. Actual Au content in the catalysts was estimated with a VARIAN VISTA-MPX atomic emission spectroscope (AES, USA).

2.3. Catalytic testing

The catalytic activity tests were carried out in a continuous-flow fixed-bed reactor consisting of a glass tube (inner diameter 0.8 cm) equipped with a CO_2 IR gas detector (FQ-W-CO_2 made in Foshan, China) [19]. 200 mg of the catalyst was loaded into the reactor. The feeding gas was 0.06 vol% formaldehyde balanced with the air generated by passing an air flow, which was previously passed through 5A zeolites and solid NaOH to remove H_2O and CO_2, through a solution of 36 wt% formaldehyde at 0 °C. The space velocity of the experiment was 6.6×104 mL h^{-1} g^{-1}. The activity of the catalysts on formaldehyde oxidization was estimated by the conversion rate of CO_2 following a formaldehyde oxidation process. The concentration of CO_2 resulting from formaldehyde oxidation was measured with the CO_2 IR gas detector to online estimate the formaldehyde oxidation. The detailed experiments were conducted following the procedures described as follows: First, the gas, which had been pre-cleaned to remove H_2O and CO_2, was continuously flowed through the Au/CeO_2 catalysts in the reactor. The reactor was then heated to 353 K to remove the substances adsorbed on the surface of the catalysts and subsequently cooled to room temperature. Next, the feeding gas containing 0.06 vol% formaldehyde was introduced into the reactor continuously. The reactor was heated to different temperatures under air flow (220 mL/min) to evaluate the temperature-dependant catalytic activity of the catalysts. The absorbed formaldehyde will be catalytically converted into CO_2 following a formaldehyde oxidation reaction. The resulting CO_2 released from the reactor due to the formaldehyde oxidation can be analyzed online with a CO_2 infrared gas analyzer.

3. Results and discussion

3.1. Colloidal crystal arrays

Colloidal crystal arrays assembled through close packing of polymer spheres into well-arranged structures could be effective templates for the creation of three-dimensional ordered macroporous materials. Depending on the sizes of the PS spheres and size distribution desired, approaches such as soap-free-emulsion polymerization and dispersion polymerization could be selectively employed [25–28]. Uniform PS spheres with narrow size distribution having average sizes around 200, 400, and 600 nm were obtained by soap-free-emulsion polymerization in our

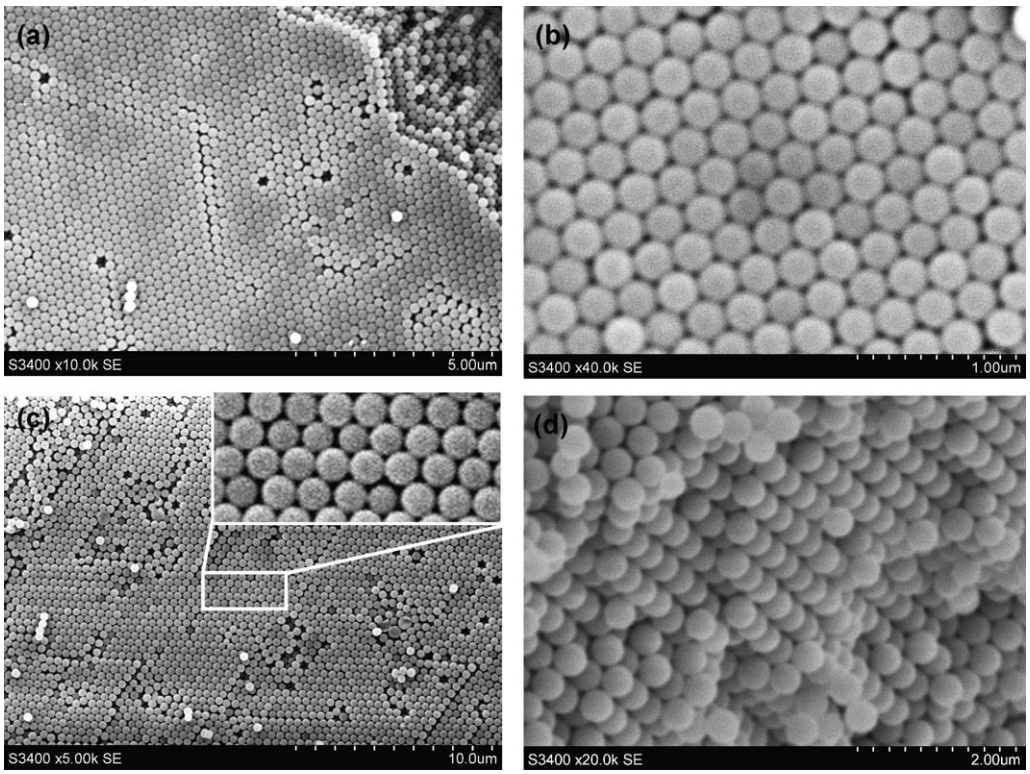

Fig. 1. SEM images showing the assembly of (a) and (b) 200 nm; and (c) and (d) 400 nm PS colloidal spheres to form three-dimensional ordered PS colloidal crystal arrays. The insert in (c) is the enlarged image of the area marked with a white rectangle.

experiments; however, this method is unfavorable for the preparation of PS spheres with uniform and narrow size distribution when PS sphere sizes are near 800 nm. Therefore, a dispersion polymerization method was used to prepare uniform PS spheres with average sizes around 800 nm. Table 1 shows the detailed reaction conditions for synthesis of monodispersed PS colloidal spheres with different average diameters. Fig. 1 shows the typical SEM images of three-dimensional ordered PS colloidal crystal arrays assembled using 200 and 400 nm PS colloidal spheres via a centrifugation method. It is observed from the lower magnification image shown in Fig. 1(a) that the PS colloidal spheres are highly uniform with narrow size distribution, and are closely packed into a highly ordered three-dimensional arrangement with long range order both parallel and perpendicular to the substrate in a large area. A face-centered-cubic (fcc) array of spheres with facets corresponding to the (1 1 1), (1 1 0), and (1 0 0) sets of planes can be clearly observed from the fractured surface at the top right of Fig. 1(a) [25,35–38]. This is further confirmed by the higher magnification image in Fig. 1(b). The average sizes of PS spheres in fcc structured colloidal crystal arrays are estimated to be around 200 nm, with almost no changes in size variation after being assembled into array geometry. Fig. 1(c) presents the SEM image of three-dimensional ordered PS colloidal crystal arrays assembled by using 400 nm PS colloidal spheres as templates. The enlarged image shown in the insert of Fig. 1(c) clearly indicates the similar assembling behavior of PS colloidal crystal arrays to that shown in Fig. 1(b). The magnification image shown in Fig. 1(d) closely displays the facet arrangement of PS spheres into a three-dimensional fcc structure. The observation for assembly of 600 and 800 nm PS spheres into three-dimensional ordered colloidal crystals is similar to that for the crystals assembled with 200 and 400 nm PS spheres. These well-arranged three-dimensional colloidal crystal arrays could be available templates for creation of 3DOM CeO_2 materials.

3.2. 3DOM CeO_2 supports

By infiltrating $Ce(NO_3)_3$ precursor into the interstices of PS colloidal crystal arrays assembled with different sized PS spheres and removing the PS sphere templates by calcination, 3DOM CeO_2 with well-defined pore sizes were achieved, as shown by the SEM images in Fig. 2. Fig. 2(a) displays 3DOM CeO_2 made by using colloidal crystal array templates assembled with 200 nm PS spheres. The image reveals the formation of CeO_2 with well-defined three-dimensional ordered macroporous structures. From the insert of partially enlarged image of Fig. 2(a), the pore sizes of 3DOM CeO_2 can be deduced to be approximately 80 nm. In comparison with original PS colloidal spheres (200 nm), the pore sizes are greatly decreased due to the calcination shrinkage. Similar large shrinkage phenomena have been observed in other 3DOM rare earth oxide systems [37]. The entire perforation of the 3DOM CeO_2 can be seen clearly from the side view of the structure. Similar phenomena are observed for the 3DOM CeO_2 synthesized by using 400 nm colloidal crystal arrays as templates, as shown in Fig. 2(b). The enlarged image shown in the insert of Fig. 2(b) suggests that the three-dimensional ordered hexagonal macropores with a pore size of approximately 130 nm decreased greatly in contrast with the original 400 nm PS spheres. Fig. 2(c) and (d) present the lower and higher magnification SEM images of the 3DOM CeO_2 fabricated by using 600 nm PS colloidal crystal arrays as templates. The interconnected networks of the ordered macropore structures can be clearly observed. The top view shown in Fig. 2(d) clearly exhibits the interconnected pores existing in the whole structure. The pores in the layer directly below the top layer are clearly visible with the holes connecting to its nearest neighbors. The pore sizes are estimated to be approximately 240 nm, with 360 nm shrinkage from 600 nm, and the fcc arrangement of PS colloidal crystals is firmly suggested. With 800 nm PS colloidal crystal arrays as templates, the 3DOM CeO_2 with larger pore sizes was obtained, as shown in Fig. 2(e) and (f). The pore sizes are

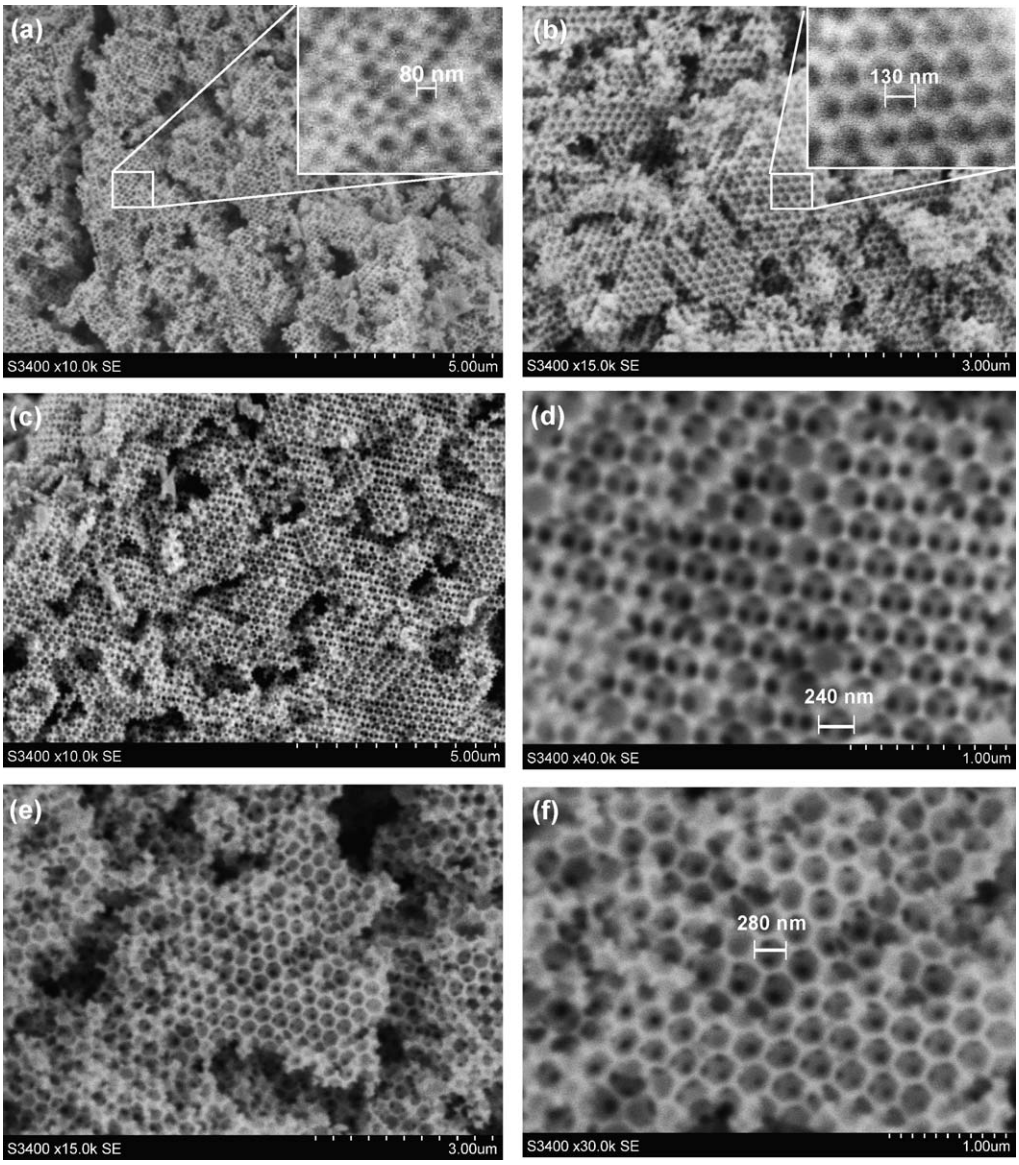

Fig. 2. SEM images of 3DOM CeO_2 supports synthesized via PS colloidal template method using (a) 200 nm, (b) 400 nm, (c and d) 600 nm and (e and f) 800 nm PS colloidal crystals as templates. Due to the shrinking during thermal removal of PS templates, the pore sizes of the obtained 3DOM CeO_2 were estimated at 80, 130, 240, and 280 nm, respectively.

estimated to be approximately 280 nm. From the above investigation, it is proved that by using different pore size PS colloidal crystal arrays as templates, 3DOM CeO_2 with variable pore sizes can be successfully fabricated.

3.3. 3DOM Au/CeO_2 catalysts

Efficient 3DOM Au/CeO_2 catalysts for enhanced catalysis of formaldehyde oxidation were synthesized with the in situ formation of a catalytic species of Au nanoparticles on 3DOM CeO_2 supports with variable pore sizes around 80, 130, 240, and 280 nm via a gas bubbling-assisted deposition precipitation approach. The SEM and TEM images of the 3DOM Au/CeO_2 catalysts with different Au loading content at ~1, 2, 3, and 4 wt% show the similar formation behaviors of Au nanoparticles with identical particle sizes. Fig. 3 presents the typical SEM and TEM images of the 3DOM Au/CeO_2 catalysts with Au loading content at ~1 wt% on 3DOM CeO_2 supports with 80 nm pore sizes. It is shown that after the in situ formation of Au nanoparticles, the Au/CeO_2 catalysts still have well-defined three-dimensional ordered macroporous structures [Fig. 3(a)]. The Au nanoparticles are well-distributed on 3DOM CeO_2 supports. The interconnected networks of 3DOM Au/CeO_2 pore voids are obvious [Fig. 3(b)], and slightly larger Au nanoparticle precipitation on top of the 3DOM Au/CeO_2 is observed, suggesting the loading of Au nanoparticles onto the 3DOM CeO_2 supports. The TEM image in Fig. 3(c) further confirms the well-defined three-dimensional ordered hexagonal structures of the Au/CeO_2 catalyst. The three-dimensional macroporous structures with overlapped pores can be clearly observed by TEM characterization [Fig. 3(d)]. Besides, the Au nanoparticles precipitated on the surface of the macroporous-structured CeO_2 supports can be observed, as suggested by the black spots with average sizes ~5 nm in Fig. 3(e). This is further confirmed by the HRTEM image in the insert of Fig. 3(e). The sizes of most Au nanoparticles formed on the surface of 3DOM supports are estimated to be around 5 nm. The HRTEM observation of the lattice fringes of d = 0.236 and 0.312 nm corresponding to Au (1 1 1) and CeO_2 (1 1 1) shown in the insert of Fig. 3(e) and (f) further confirms the existence of small Au nanoparticles on 3DOM CeO_2 supports.

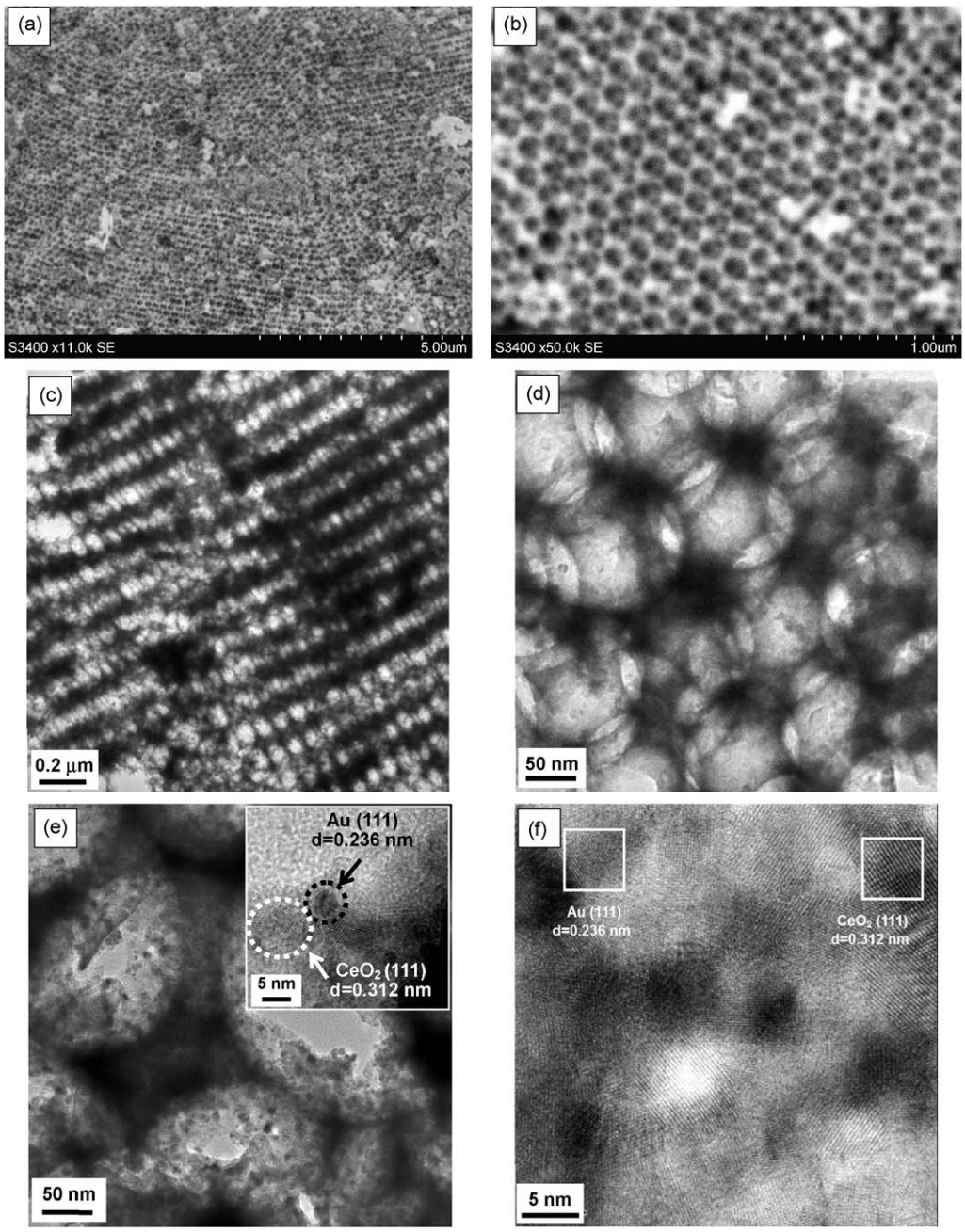

Fig. 3. SEM (a and b), TEM (c–e) and HRTEM (insert of e and f) images of 3DOM Au ca. 1 wt%/CeO_2 synthesized via a gas bubbling-assisted deposition precipitation method through in situ formation of Au nanoparticles on a 80 nm pore size 3DOM CeO_2 support. The black and white circles in the insert of (e) and the white rectangles in (f) clearly showing the lattice fringes of Au (1 1 1) and CeO_2 (1 1 1) firmly suggest the formation of small Au nanoparticles on 3DOM CeO_2 support.

To verify the existence of Au in the 3DOM Au/CeO_2 catalysts, energy dispersive X-ray (EDX) analysis of 3DOM Au ~1 wt%/CeO_2 catalysts was carried out. It was found that the representative peaks corresponding to Ce, Au, C, and O elements are detected, which confirms the formation of CeO_2 and the existence of Au element in the 3DOM Au/CeO_2 catalysts. The result is consistent with the TEM observation.

To confirm the formation and phase structures of the 3DOM Au/CeO_2 catalyst, XRD characterization was performed. The 3DOM CeO_2 supports with 80 and 130 nm pore sizes and 3DOM Au/CeO_2 catalysts with 80 and 130 nm pore sizes were comparatively characterized, as typical XRD patterns are shown in Fig. 4. The XRD patterns clearly illustrate the formation of CeO_2 [Fig. 4 (a and c)] and Au/CeO_2 catalysts [(Fig. 4 (b and d)], and the phase structures of all catalysts can be indexed to cubic phased CeO_2 (JCPDS: 34-394), as characteristic diffraction peaks with 2θ at 28.50, 33.08, 47.49, 56.34, and 76.70 correspond to (1 1 1), (2 0 0), (2 2 0), (3 1 1), and (3 3 1) lattices of cubic structured CeO_2, respectively. The XRD patterns of 3DOM CeO_2 and Au/CeO_2 display a broad diffraction feature, implying the macroporous structures of the catalysts [33]. No characteristic diffraction peaks belonging to Au nanoparticles were detected, possibly due to the good distribution and low loading concentration of Au in the catalysts, as the similar phenomenon has been observed in ceria supported Au nanoparticles catalysts [19].

3.4. Catalytic performance on formaldehyde oxidation

The performance of 3DOM CeO_2 supports and 3DOM Au ~1 wt%/CeO_2 catalysts with pore sizes at 80 and 130 nm in

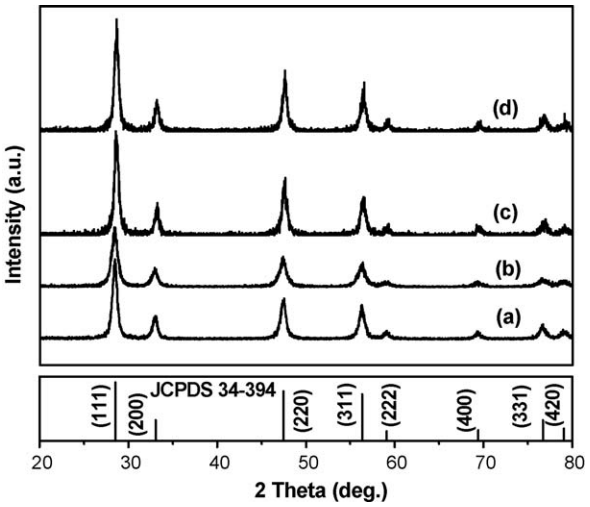

Fig. 4. XRD patterns of (a) 3DOM CeO_2 catalyst with 130 nm pore size, (b) 3DOM Au ~1 wt%/CeO_2 with 130 nm pore size (60 °C drying), (c) 3DOM CeO_2 catalyst with 80 nm pore size, (d) 3DOM Au ~1 wt%/CeO_2 with 80 nm pore size (60 °C drying).

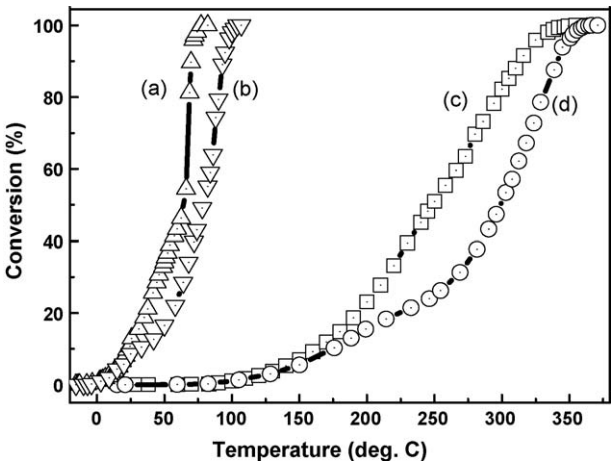

Fig. 5. Catalytic activity of (a) 3DOM Au ~1 wt%/CeO_2 (80 nm pore size), (b) 3DOM Au ~1 wt%/CeO_2 (130 nm pore size), (c) 3DOM CeO_2 (80 nm pore size), (d) 3DOM CeO_2 (130 nm pore size) catalysts on formaldehyde oxidation.

formaldehyde catalytic oxidation was tested, and the curves of catalytic activity at different testing temperatures are indicated in Fig. 5. Relatively low catalytic activity is shown for 3DOM CeO_2 supports with 80 and 130 nm pore sizes with a 100% formaldehyde conversion rate at temperatures around 355 and 370 °C, respectively. In contrast, after the Au nanoparticles were loaded on the 3DOM CeO_2 supports, the catalytic activity of the 3DOM Au/CeO_2 catalysts was greatly enhanced, with a 100% formaldehyde conversion rate at temperatures around 75 °C for 80 nm pore size and 90 °C for 130 nm pore size, much lower than temperatures previously reported [10,13,15,19,20]. The 3DOM Au/CeO_2 catalyst with 80 nm pore sizes shows higher catalytic activity (with around 15 °C deviation) than the 3DOM Au/CeO_2 catalyst with 130 nm pore sizes. Table 2 listed the pore sizes, Au contents and BET surface area of the catalysts for HCHO oxidation performance. According to the Table 2 for the BET measurements of catalysts, the surface areas of 3DOM CeO_2 and Au/CeO_2 catalysts with 80 nm pore sizes are estimated to be around 41.1 and 11.2 m^2/g, thus decreasing greatly with Au nanoparticle loading. For 3DOM CeO_2 and Au/CeO_2 catalysts with 130 nm pore sizes, the surface area correspondingly decreases from 37.8 to 9.3 m^2/g. However, the Au/CeO_2 catalysts with 80 nm pore sizes have slightly larger surface areas. Based on the AES measurement for 3DOM Au ~1 wt%/CeO_2 catalysts with pore sizes at 80 and 130 nm, the actual Au contents are around 0.42% and 0.45% respectively (Table 2), relatively close even though the pore sizes of CeO_2 supports are different.

In order to investigate the effects of pore size on catalytic activity, the catalytic activity of 3DOM Au ~1 wt%/CeO_2 catalysts with 80, 130, and 280 nm pore sizes were comparatively studied, and the catalytic performance curves are shown in Fig. 6. It can be seen from Fig. 6 that the 3DOM Au ~1 wt%/CeO_2 catalyst with

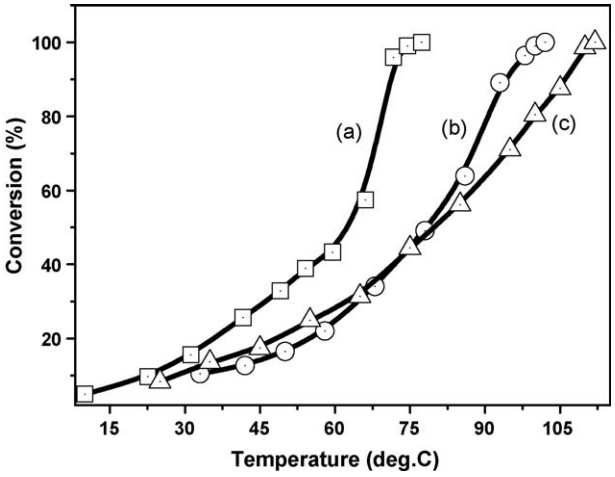

Fig. 6. Comparison of catalytic activity of Au/CeO_2 catalysts with different pore sizes on formaldehyde oxidation, (a) 3DOM Au ~1 wt%/CeO_2 (80 nm pore size), (b) 3DOM Au ~1 wt%/CeO_2 (130 nm pore size), (c) 3DOM Au ~1 wt%/CeO_2 (280 nm pore size).

80 nm pores displays the highest catalytic activity on formaldehyde oxidation, as it has the highest surface area and the small pore size (Table 2) may lead to more uniform distribution of small Au nanoparticles, which may account for the improvement of catalytic capability. Fig. 7 shows the effect of Au content in the 3DOM Au/CeO_2 catalyst (80 nm pore size) on catalytic activity for formaldehyde oxidation. The 3DOM Au/CeO_2 catalysts with theoretical Au content at ~1, 2, 3, and 4 wt% were tested. It is shown that the 3DOM Au/CeO_2 catalyst with Au content at ~3 wt% had the most

Table 2
The pore sizes, Au contents and BET surface areas of the catalysts.

Catalysts	Pore sizes (nm)	Au contents		BET surface area (m^2/g)
		Theoretical	Actual	
3DOM CeO_2 (200 nm PS as templates)	~80			41.1
3DOM Au/CeO_2 (200 nm PS as templates)	~80	1%	0.42%	11.2
		3%	0.56%	
3DOM CeO_2 (400 nm PS as templates)	~130			37.8
3DOM Au/CeO_2 (400 nm PS as templates)	~130	1%	0.45%	9.3
3DOM Au/CeO_2 (800 nm PS as templates)	~280	1%	0.45%	8.7

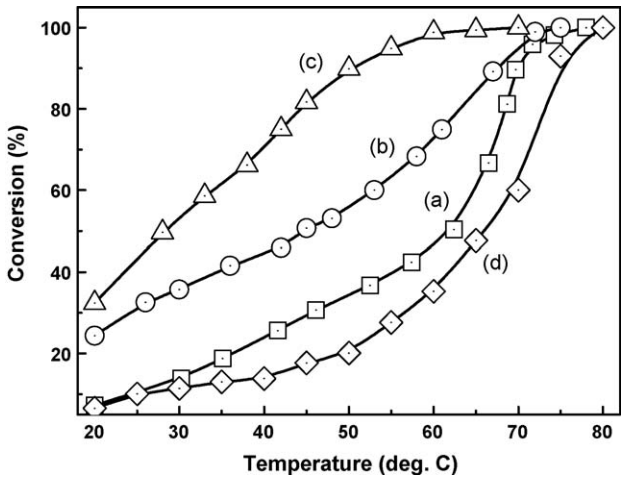

Fig. 7. Comparison of catalytic activity of 3DOM Au/CeO_2 catalysts (80 nm pore size) with different theoretical Au loading contents on formaldehyde oxidation, (a) Au ~1 wt%/CeO_2, (b) Au ~2 wt%/CeO_2, (c) Au ~3 wt%/CeO_2, (d) Au ~4 wt%/CeO_2.

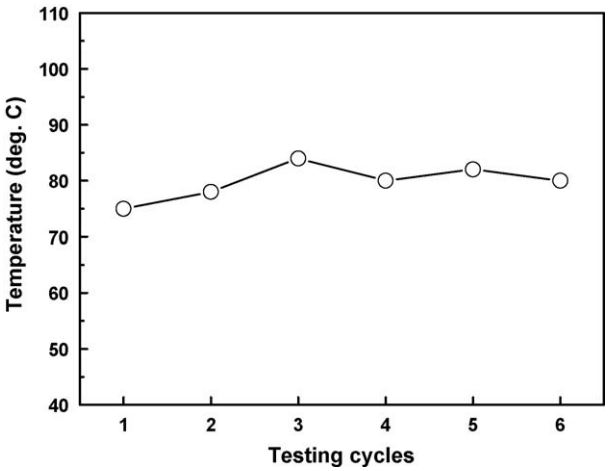

Fig. 9. The catalytic stability of 3DOM Au ~3 wt%/CeO_2 with six testing cycles.

efficient catalytic activity with 30% conversion of formaldehyde at room temperature and 100% conversion at 75 °C. The AES characterization (Table 2) shows that the actual Au content in this catalyst is around 0.56 wt%, the highest in all the 3DOM Au/CeO_2 catalysts (80 nm pore size), which may account for its highest catalytic capability.

To evaluate the effects of annealing treatment on the catalytic activity of the catalysts, the catalytic activity of 3DOM Au ~3 wt%/CeO_2 catalysts (80 nm pore size) obtained at different reaction temperatures of 60 °C drying, 200 and 400 °C annealing were tested, as their catalytic curves were shown in Fig. 8(a)–(c), respectively. The 3DOM Au ~3 wt%/CeO_2 catalysts treated at 60, 200, and 400 °C exhibit the catalytic activity with 100% conversion of formaldehyde at the temperatures of 75, 80, and 120 °C, respectively. This phenomenon suggests that the annealing treatment of the catalysts may cause the loss of catalytic activity.

The catalytic stability of the 3DOM Au/CeO_2 catalysts was also evaluated in by carrying out the catalytic performance of 3DOM Au/CeO_2 catalyst with six testing cycles. Fig. 9 indicated the results of six repeated cycles of formaldehyde oxidation on 3DOM Au ~3 wt%/CeO_2 catalysts. The tests implied that the 3DOM Au ~3 wt%/CeO_2 catalysts had relatively stable catalytic performances with 100% conversion of formaldehyde oxidation at the temperature in 75–85 °C. The temperature for 100% conversion of formaldehyde oxidation for the fresh catalyst kept at 75 °C, but with a little fluctuation between 75 and 80 °C for the repeated catalysts, suggesting the catalytic stability of 3DOM Au~/CeO_2 catalyst.

3.5. XPS measurements

The XPS characterization was applied to determine the 3DOM Au/CeO_2 catalyst composition and Au valance. The wide scanning XPS spectrum of the 3DOM Au/CeO_2 catalyst is illustrated in Fig. 10. It can be seen from the spectrum that the elements Ce, O, and Au exist in the catalyst, as the XPS peaks of Ce3d, Ce4p, Ce4d, O1s, and Au4f are clearly observed, suggesting the formation of Au/CeO_2. In contrast with XRD characterization, in which no characteristic peaks belonging to Au nanoparticles are detected, the XPS measurements firmly suggest the formation of Au nanoparticles onto 3DOM CeO_2 supports. However, the Au4f signal from Au nanoparticles is relatively weaker, implying small amounts of Au exist on surface of catalyst supports. The magnified XPS spectra for the 3DOM Au ~1 wt%/CeO_2 catalysts fabricated via different post-treatments are shown in Fig. 11. It is reported that the typical binding energies of $Au4f_{7/2}$ for Au (Au^0), Au_2O_3, and

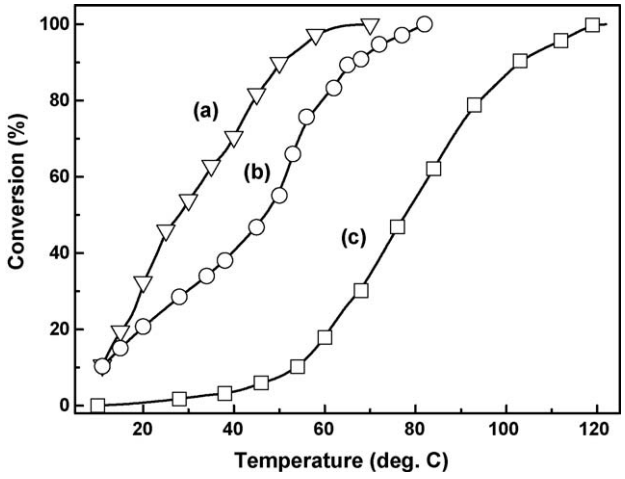

Fig. 8. Comparison of catalytic activity of 3DOM Au ~3 wt%/CeO_2 catalysts (80 nm pore size) obtained at different reaction temperatures on formaldehyde oxidation, (a) 60 °C drying, (b) 200 °C annealing and (c) 400 °C annealing.

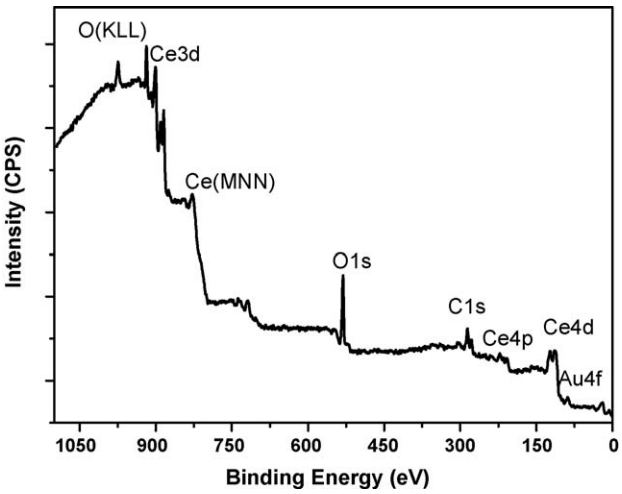

Fig. 10. Wide scanning XPS spectrum of Au ~1 wt%/CeO_2 catalyst.

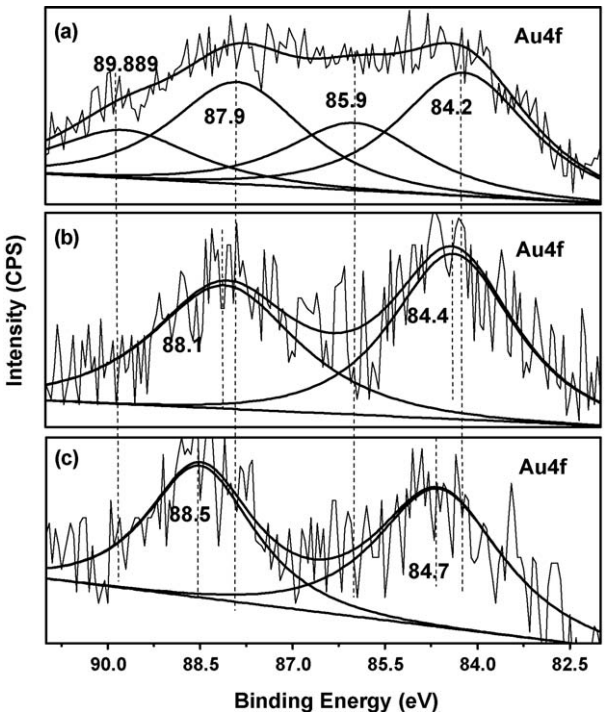

Fig. 11. Au4f XPS spectra of 3DOM Au ~1 wt%/CeO_2 catalysts with 80 nm pore sizes (a) as-prepared by drying at 60 °C before use for formaldehyde oxidation, (b) after use for formaldehyde oxidation, (c) synthesized by calcination of as-prepared sample at 400 °C.

$Au(OH)_3$ (Au^{3+}) are located at 83.9, 86.3, 87.7 eV, respectively, while those of $Au4f_{5/2}$ for Au (Au^0), Au_2O_3, and $Au(OH)_3$ (Au^{3+}) correspond to 87.7, 89.6, and 91.4 eV, respectively [19,20,38]. It was found in our XPS measurements that the Au valence in 3DOM Au/CeO_2 catalysts before and after use for formaldehyde oxidation is quite different. In the freshly prepared 3DOM Au/CeO_2 catalyst, four peaks [Fig. 11(a)] are found, which could be indexed to Au^0 ($Au4f_{7/2}$ and $Au4f_{5/2}$ located at 84.2 and 87.9 eV, respectively) and Au^{3+} ($Au4f_{7/2}$ and $Au4f_{5/2}$ observed at 85.9 and 89.9 eV, respectively), suggesting the coexistence of Au^0 and Au^{3+} in the catalyst. After the formaldehyde oxidation over the catalyst under the investigating temperature range of 20–200 °C, the Au valence state in the catalyst changed. The XPS peaks belonging to Au^{3+} disappeared, and only two peaks located at 84.4 and 88.1 eV indexed to $Au4f_{7/2}$ and $Au4f_{5/2}$ of Au^0 are detectable [Fig. 11(b)]. This indicates the transformation of Au^{3+} to Au^0 during the catalytic oxidation process. The same phenomena are observed for the 3DOM catalyst thermally treated at 400 °C. Only two XPS peaks belonging to Au^0 ($Au4f_{7/2}$ at 84.7 and $Au4f_{5/2}$ at 88.57 eV) were measured [Fig. 11(c)]. It is revealed that thermal treatment of oxide-supported Au catalysts could lead to the reduction of Au^{3+} into Au^0 [19,20,38]. The mixed valence states of Au^{3+} and Au^0 or the intermediate valence states $Au^{\delta+}$ in Au/CeO_2 catalyst are believed to enhance catalytic activity. This is the case in our investigation, since the freshly prepared 3DOM Au/CeO_2 catalyst, in which Au^{3+} and Au^0 co-exist, shows higher catalytic activity than the post-treatment 3DOM Au/CeO_2 catalyst (Fig. 8), which contains only Au^0, though the catalysts before and after thermal treatment keep the same structure, pore size, and geometry (Figure S1 in supporting information). Therefore, due to the unique porous structure inducing well-distributed Au nanoparticle loading and the existence of mixed valence states of Au^{3+} and Au^0 in the catalysts, our 3DOM Au/CeO_2 catalysts show the enhanced catalytic activity than the Au/CeO_2 catalysts without porous structures.

4. Conclusions

In this paper, novel 3DOM Au/CeO_2 catalysts with variable pore sizes from 80 to 280 nm were developed via template-directed synthesis of 3DOM CeO_2 supports by using colloidal crystal PS spheres as templates following Au nanoparticle catalyst in situ formation on 3DOM CeO_2 supports by a gas bubbling-assisted deposition precipitation approach. The 3DOM Au/CeO_2 catalysts show unique 3DOM structures with interconnected networks of spherical voids favoring less aggregation and good distribution of small Au nanoparticles, which induces the enhanced catalytic capability for formaldehyde oxidation with 100% formaldehyde conversion at temperature as low as ~75 °C, approximately 25 °C lower than previously reported Au/CeO_2 catalysts without porous structure. The catalytic capability of 3DOM Au/CeO_2 catalysts with 80 nm pores shows the highest catalytic activity among all the investigated catalysts with variable pore sizes. The Au good distribution, higher Au loading content and the mixed Au valence states of Au^{3+} and Au^0 in freshly prepared 3DOM Au/CeO_2 catalysts may be the key factors for the enhancement of catalytic efficiency for formaldehyde oxidation. The superior catalytic performance of 3DOM Au/CeO_2 catalysts on formaldehyde oxidation may find potential applications in indoor formaldehyde decontamination and industrial catalysis.

Acknowledgement

We gratefully acknowledge the financial support from National Natural Science Foundation of China (20601012), Inner Mongolia University (Nanomaterials Lab: 10013-121008, High Level Talent Program: 206043, 513 Talent Program: 206077), and the Educational Department of Inner Mongolia (NJZY07011).

Appendix A. Supplementary data

Supplementary data associated with this article can be found, in the online version, at doi:10.1016/j.apcatb.2009.05.001.

References

[1] U.S. EPA, Characterizing Air Emissions from Indoor Sources, EPA report: EPA/600/F-95/005, U.S. Environmental Protection Agency, Washington, DC, 1995.
[2] Agency for Toxic Substance and Disease Registry, Public Health Service, U.S. Department of Health and Human Services, Toxicological Profile for Formaldehyde, NTIS Accession No. PB99-166654, 1991, p. 451.
[3] International Agency for Research on Cancer, IARC Monographs on the Evaluation of the Carcinogenic Risk of Chemicals to Humans, Some Industrial Chemicals and Dyestuffs, Lyon, France, 29, 1982, p. 416.
[4] E.A. Batista, T. Iwasita, Langmuir 22 (2006) 7912.
[5] R.B. de Lima, M.P. Massafera, E.A. Batista, T. Iwasita, J. Electroanal. Chem. 603 (2007) 142.
[6] C. Lahousse, A. Bernier, P. Grange, B. Delmon, P. Papaefthimiou, T. Ioannides, X. Verykios, J. Catal. 178 (1998) 214.
[7] R. Spinici, M. Faticanti, P. Marini, S. De Rossi, P. Porta, J. Mol. Catal. A 197 (2003) 147.
[8] Y. Sun, Y. Shen, M. Jia, R. Hu, Acta Physico-Chim. Sinica 15 (1999) 720.
[9] C. Zhang, H. He, Catal. Today 126 (2007) 345.
[10] X. Tang, J. Chen, Y. Li, Yong. Li, Y. Xu, W. Shen, Chem. Eng. J. 18 (2006) 119.
[11] S. Imamura, Y. Uematsu, K. Utani, T. Ito, Ind. Eng. Chem. Res. 30 (1991) 18.
[12] K.T. Chuang, B. Zhou, S.M. Tong, Ind. Eng. Chem. Res. 33 (1994) 1680.
[13] M.C. Álvarez-Galván, B. Pawelec, V.A. de la Peña O'Shea, J.L.G. Fierro, P.L. Arias, Appl. Catal. B: Environ. 51 (2004) 83.
[14] C. Zhang, H. He, K. Tanaka, Catal. Commun. 6 (2005) 211.
[15] M.C. Álvarez-Galván, V.A. de la Peña O'Shea, J.L.G. Fierro, P.L. Arias, Catal. Commun. 4 (2003) 223.
[16] X. Tang, J. Chen, X. Huang, Y. Xu, W. Shen, Appl. Catal. B: Environ. 81 (2008) 115.
[17] M. Haruta, S. Tsubota, T. Kobayashi, H. kageyama, J. Catal. 144 (1993) 175.
[18] M. Haruta, Y. Yamada, T. Kobayashi, T. Iijima, J. Catal. 115 (1989) 301.
[19] Y. Shen, X. Yang, Y. Wang, Y. Zhang, H. Zhu, L. Gao, M. Jia, Appl. Catal. B: Environ. 79 (2008) 142.
[20] C. Li, Y. Shen, M. Jia, S. Sheng, M.O. Adebajo, H. Zhu, Catal. Commun. 9 (2008) 355.
[21] M. Haruta, Catal. Today 36 (1997) 153.
[22] G.C. Bond, Catal. Today 72 (2002) 5.

[23] H.H. Kung, M.C. Kung, C.K. Costello, J. Catal. 216 (2003) 425.
[24] N. Lopez, T.V.W. Janssens, B.S. Clausen, Y. Xu, M. Mavrikakis, T. Bligaard, J.K. Nørskov, J. Catal. 223 (2004) 232.
[25] B.T. Holland, C.F. Blanford, T. Do, A. Stein, Chem. Mater. 11 (1999) 795.
[26] B.T. Holland, C.F. Blanford, A. Stein, Science 281 (1998) 538.
[27] J.H. Kim, M. Chainey, M.S. El-Aasser, J.W. Vanderhoff, J. Polym. Sci. Part A: Polym. Chem. 27 (1989) 3187.
[28] H. Kawaguchi, Prog. Polym. Sci. 25 (2000) 1171.
[29] A.J. Paine, Macromolecules 23 (1990) 3109.
[30] K.P. Lok, C.K. Ober, Can. J. Chem. 63 (1985) 206.
[31] C.K. Ober, K.P. Lok, Macromolecules 20 (1987) 268.
[32] A. Stein, Microporous Mesoporous Mater. 44∼45 (2001) 227.
[33] Q. Wu, Y. Shen, J. Liao, Y. Li, Mater. Lett. 58 (2004) 2688.
[34] S. Li, J. Zheng, W. Yang, Y. Zhao, Y. Liu, J. Porous Mater 15 (2008) 589.
[35] H. Cong, W. Cao, Langmuir 19 (2003) 8177.
[36] G.I.N. Waterhouse, M.R. Waterland, Polyhedron 26 (2007) 356.
[37] Y. Zhang, Z. Lei, J. Li, S. Lu, New J. Chem. 25 (2001) 1118.
[38] E.D. Park, J.S. Lee, J. Catal. 186 (1999) 1.